



Publication Year	2019
Acceptance in OA @INAF	2024-02-12T15:10:49Z
Title	Compton-thick AGNs in the NuSTAR Era. V. Joint NuSTAR and XMM-Newton by Spectral Analysis of Three Soft-gamma Candidate C 100-month Catalog
Authors	MARCHESI, STEFANO; Ajello, M; Zhao, X.; COMASTRI, Andrea; LA PAROLA, VALENTINA; et al.
DOI	10.3847/1538-4357/ab340a
Handle	http://hdl.handle.net/20.500.12386/34746
Journal	THE ASTROPHYSICAL JOURNAL
Number	882



Compton-thick AGNs in the *NuSTAR* Era. V. Joint *NuSTAR* and *XMM-Newton* Spectral Analysis of Three “Soft-gamma” Candidate CT-AGNs in the *Swift*/BAT 100-month Catalog

S. Marchesi¹ , M. Ajello¹ , X. Zhao¹ , A. Comastri² , V. La Parola³ , and A. Segreto³
¹Department of Physics and Astronomy, Clemson University, Kinard Lab of Physics, Clemson, SC 29634, USA
²INAF—Osservatorio di Astrofisica e Scienza dello Spazio di Bologna, Via Piero Gobetti, 93/3, I-40129, Bologna, Italy
³INAF—Istituto di Astrofisica Spaziale e Fisica Cosmica, Via U. La Malfa 153, I-90146 Palermo, Italy
 Received 2019 May 4; revised 2019 July 12; accepted 2019 July 18; published 2019 September 13

Abstract

We present the joint *NuSTAR* and *XMM-Newton* spectral analysis in the 0.6–70 keV band of three candidate Compton-thick (CT-) active galactic nuclei (AGNs) selected in the 100-month *Swift*-BAT catalog. These objects were previously classified as CT-AGNs based on low-quality *Swift*-X-ray Telescope (XRT) and *Swift*-Burst Alert Telescope (BAT) data, and had soft photon indices ($\Gamma > 2.2$) that suggested a potential overestimation of the line-of-sight column density ($N_{\text{H,LOS}}$). Thanks to the high-quality *NuSTAR* and *XMM-Newton* data we were able to determine that in all three objects the photon index was significantly overestimated, and two out of three sources are reclassified from CT to Compton thin, confirming a previously observed trend, i.e., that a significant fraction of BAT-selected, candidate CT-AGNs with poor soft X-ray data are reclassified as Compton thin when the *NuSTAR* data are added to the fit. Finally, thanks to both the good *XMM-Newton* spatial resolution and the high *NuSTAR* and *XMM-Newton* spectral quality, we found that the third object in our sample was associated to the wrong counterpart: the correct one, 2MASX J10331570+5252182, has redshift $z = 0.14036$, which makes it one of the very few candidate CT-AGNs in the 100 months BAT catalog detected at $z > 0.1$, and a rare CT quasar.

Key words: galaxies: active – galaxies: nuclei – X-rays: galaxies

1. Introduction

The study in the X-rays of heavily obscured active galactic nuclei (AGNs) and, more specifically, of the obscuring material commonly defined as “torus” and constituted of dust and cold molecular gas surrounding the accreting supermassive black holes (SMBHs) in the center of the galaxies, has been significantly improved by the launch of the Nuclear Spectroscopic Telescope Array (hereafter *NuSTAR*; Harrison et al. 2013). In fact, *NuSTAR* has excellent sensitivity over the 3–78 keV range and is the first telescope with focusing optics at >10 keV. This makes it an ideal instrument to study heavily obscured AGNs, because their observed X-ray emission peaks at ~ 30 –50 keV (see, e.g., Antonucci 1993; Comastri et al. 1995; Gilli et al. 2007; Ajello et al. 2008), in the so-called “Compton hump,” while little to no photons at energies below 5 keV escape the obscuring material (see, e.g., Murphy & Yaqoob 2009; Brightman & Nandra 2011; Koss et al. 2016).

Over the years, *NuSTAR* targeted many well-known Compton-thick (CT)-AGNs in the nearby universe ($z \leq 0.1$), making it possible to characterize them with unprecedented accuracy (see, e.g., Baloković et al. 2014; Puccetti et al. 2014, 2016; Annuar et al. 2015; Bauer et al. 2015; Brightman et al. 2015; Koss et al. 2015; Rivers et al. 2015; Masini et al. 2016; Ursini et al. 2018; Zhao et al. 2019a, 2019b), using Monte Carlo radiative transfer codes specifically developed to fit the X-ray spectra of heavily obscured AGNs (e.g., Ikeda et al. 2009; Murphy & Yaqoob 2009; Yaqoob et al. 2010; Brightman & Nandra 2011; Yaqoob 2012; Liu & Li 2014; Furui et al. 2016; Baloković et al. 2018). These models are more refined than simple phenomenological ones, and allow one to measure important parameters, such as the torus covering factor, f_c , and the torus average column density, $N_{\text{H,tor}}$. To be used effectively, however, these models require an

excellent spectral statistics in the 2–50 keV band, a condition that cannot be satisfied either by one of the several 0.3–10 keV facilities or by the *Swift*-Burst Alert Telescope (BAT).

In Marchesi et al. (2018, 2019, M18, M19 hereafter) we analyzed the combined 2–100 keV spectra of 35 candidate nearby (average redshift $\langle z \rangle = 0.03$) CT-AGNs, i.e., all the 100 months BAT candidate CT-AGNs having archival *NuSTAR* data. 2–10 keV data have been obtained using archival *XMM-Newton*, *Chandra*, and *Swift*-X-ray Telescope (XRT) data. We discovered a systematic trend to artificially overestimate the line-of-sight (LOS) column density and the steepness of the spectrum when only the 2–10 keV and the *Swift*-BAT data are included in the fit. This effect is variability- and model-independent and stronger in sources with low statistics (net cts < 100) in the 0.3–10 keV band, i.e., mostly objects with only a *Swift*-XRT or a short (< 10 ks) *Chandra* observation available. In these objects, the LOS column density is overestimated, on average, by $\sim 45\%$, while the average photon index variation is $\Delta\Gamma = 0.25$. No significant trend is instead observed in sources with deep (≥ 20 ks) *XMM-Newton* observations. As a consequence, only about half ($54_{-13}^{+10}\%$) of the candidate nearby CT-AGNs already reported in the literature are confirmed as bona fide CT-AGNs.

This result has important implications for our understanding of the cosmic X-ray background (CXB) and the total accretion history of the universe. For example, based on our results, the observed CT-AGN fraction in the 70 months *Swift*-BAT catalog ($7.6_{-2.1}^{+1.1}\%$ Ricci et al. 2015) decreases to $6.0_{-0.5}^{+0.4}\%$ and potentially even down to $\sim 4\%$, extrapolating the results of our work to the population of candidate CT-AGNs with no *NuSTAR* data available. Notably, the low- z observed and intrinsic CT-AGN fractions play an important role in SMBH population synthesis and CXB models (see, e.g., Gilli et al. 2007; Treister et al. 2009;

Ballantyne et al. 2011; Ueda et al. 2014; Ananna et al. 2019), leaving the total contribution of CT-AGNs to the CXB still debated.

Within the framework of a broader project in which we aim to characterize the whole CT-AGN population of nearby, *Swift*-BAT-selected candidate CT-AGNs, in this work we therefore study the joint *NuSTAR*–*XMM-Newton* spectrum of the three candidate CT-AGNs selected in the 100 months BAT catalog (Marchesi et al. 2019) having spectra with less than 35 counts in the 2–10 keV band and best-fit $\Gamma \geq 2.2$.

The paper is organized as follows: in Section 2 we present the sample used in this work and we describe the data reduction and spectral extraction process for both *NuSTAR* and the 0.3–10 keV observations. In Section 3 we describe the models used to perform the spectral fitting. In Section 4 we report the results of the spectral analysis and an extended discussion on the reassociation of one of the three sources in our sample. Finally, we discuss our results and report our conclusions in Section 5. All reported errors are at a 90% confidence level, if not otherwise stated.

2. Sample Selection and Data Reduction

The three sources analyzed in this work (ESO 244–IG 030, $z = 0.0256$; ESO 317–G 041, $z = 0.0193$; and 2MASX J10331570+5252182, $z = 0.14036$) have been selected from the Palermo BAT 100 months catalog⁴. The data have been processed with the BAT_IMAGER code (Segreto et al. 2010), and the spectra are background subtracted and exposure-averaged. We use the standard *Swift*-BAT spectral redistribution matrix.⁵

All the sources are reported to be candidate CT-AGNs (Ricci et al. 2015), but they also have a particularly soft best-fit photon index ($\Gamma \geq 2.2$, see Table 1): while similar photon indices are not necessarily unphysical, the typical AGN photon index is usually significantly harder ($\Gamma \sim 1.4$ – 2.0 ; see, e.g., Nandra & Pounds 1994; Risaliti & Elvis 2004; Ueda et al. 2014; Marchesi et al. 2016). Furthermore, given the known degeneracy between Γ and the LOS column density, $N_{\text{H},z}$, if the photon index value turns out to be overestimated, it is likely that $N_{\text{H},z}$ could also be overestimated, potentially moving these sources from the CT to the Compton thin regime. Notably, all three sources had only been observed in the 0.5–10 keV band with *Swift*-XRT and have poor count statistics (15–25 net counts; see Table 1), thus Γ and $N_{\text{H},z}$ both had relatively large (30%–40%) uncertainties.

To properly assess the X-ray spectral properties of these three AGNs we proposed for a joint, 20 ks *XMM-Newton*, 30 ks *NuSTAR* follow-up. Our proposal was accepted (*NuSTAR* GO Cycle 4, proposal ID: 4253; PI S. Marchesi) and the observations took place between 2018 May and June. We report a summary of the observations in Table 1.

The *XMM-Newton* data were reduced using the Science Analysis System (SAS) v16.1.0⁶ (Jansen et al. 2001) packages and adopting standard procedures. We extracted the source spectra from a 15'' circular region. If the source is observed on-axis, as it is the case for the three sources studied in this work, such a radius is equivalent to $\sim 70\%$ of the encircled energy fraction at 5 keV for all the three *XMM-Newton* 0.5–10 keV

cameras (MOS1, MOS2, and pn). The background spectra were instead extracted from a circular region having radius $r = 45''$. For all sources, the background spectra were extracted from a part of the charge-coupled device (CCD) located near the source and not contaminated by other objects. Finally, each spectrum has been binned with at least 20 counts per bin.

We point out that the *Swift*-BAT source 4BPCJ1033.4+5252 (i.e., source SWIFTJ1033.8+5257 in Ricci et al. 2015) was originally associated to the galaxy SDSS J103315.71+525217.8 at $z = 0.0653$, a source located at $\sim 10''$ from 2MASX J10331570+5252182. As can be seen in Figure 1, however, the *XMM-Newton* centroid is closer to the southern source, i.e., 2MASX J10331570+5252182 ($z = 0.14036$), thus supporting the hypothesis that this is instead the correct counterpart. We will further strengthen this claim in Section 4.3, where we report the joint *NuSTAR* and *XMM-Newton* analysis of 4BPCJ1033.4+5252.

Finally, for all the objects the data retrieved for both *NuSTAR* Focal Plane Modules (FPMA and FPMB; Harrison et al. 2013) were processed using the *NuSTAR* Data Analysis Software v1.5.1. The event data files were calibrated running the *nupipeline* task using the response file from the Calibration Database v. 20181030. With the *nuproducts* script we generated both the source and background spectra, and the ancillary and response matrix files. For both focal planes, we used a circular source extraction region with a radius chosen to maximize the spectral signal-to-noise ratio⁷ (S/N), and centered on the target source; for the background we used the same extraction region positioned far from any source contamination in the same frame. The *NuSTAR* spectra have then been grouped with at least 20 counts per bin, and cover the energy range from 3 to 50–70 keV, depending on the quality of the data.

3. Spectral Fitting Procedure

The spectral fitting procedure was performed using the XSPEC software (Arnaud 1996); the Galactic absorption values is the one measured by Kalberla et al. (2005). We used Anders & Grevesse (1989) cosmic abundances, fixed to the solar value, and the Verner et al. (1996) photoelectric absorption cross section. The data are fitted between 0.6 and 70 keV in ESO 244–IG 030 and 2MASX J10331570+5252182, while in ESO 317–G 041 we select the 3–70 keV energy range to avoid an artificial flattening in the best-fit photon index (see Section 4.2 for further details).

The spectra are fitted using two Monte Carlo radiative transfer codes specifically developed to characterize the spectra of heavily obscured AGNs: MYTORUS (Murphy & Yaqoob 2009; Yaqoob 2012; Yaqoob et al. 2015), used both in its “coupled” and in its “decoupled” configuration, and borus02 (Baloković et al. 2018).

3.1. MYTORUS

In MYTORUS, the obscuring material is toroidally shaped and azimuthally symmetric; the torus half-opening angle is fixed to $\theta_{\text{OA}} = 60^\circ$ (i.e., the torus covering factor is fixed to $f_c = \cos(\theta_{\text{OA}}) = 0.5$), while the angle between the torus axis and the observer is a free parameter, which varies in the range $\theta_{\text{obs}} = [0-90]^\circ$.

⁴ http://bat.ifc.inaf.it/100m_bat_catalog/100m_bat_catalog_v0.0.htm

⁵ Available at <http://heasarc.gsfc.nasa.gov/docs/heasarc/caldb/data/swift/bat/index.html>.

⁶ <http://xmm.esa.int/sas>

⁷ 40'' for ESO 244–IG 030, 60'' for ESO 317–G 041, 50'' for 2MASX J10331570+5252182, and 60'' for 2MASX J10313591–4206093, which we analyze in the Appendix.

Table 1
Properties of the Candidate CT-AGNs Analyzed in This Work

4PBC ID	Source Name	R.A.	Decl.	z	$N_{\text{H},z,\text{Swi}}$	Γ_{Swi}	cts	Telescope	ObsID	Date	Exp	Rate
(1)	(2)	(deg)	(deg)	(5)	(6)	(7)	(8)	(9)	(10)	(11)	(ks)	(cts s ⁻¹)
(1)	(2)	(3)	(4)	(5)	(6)	(7)	(8)	(9)	(10)	(11)	(12)	(13)
J0129.8–4218	ESO 244–IG 030	22.46346	–42.32647	0.0256	24.2 ^{+0.4} _{–0.2}	2.45 ^{+0.35} _{–0.40}	15	XMM	0830500101	2018 May 23	66.6	0.018
								<i>NuSTAR</i>	60468001002	2018 May 23	60.1	0.015
J1031.5–4203	ESO 317–G 041	157.84633	–42.06061	0.0193	24.3 ^{+0.4} _{–0.2}	2.20 ^{+0.27} _{–0.22}	12	XMM	0830500201	2018 May 27	75.8	0.003
								<i>NuSTAR</i>	60468002002	2018 May 27	61.3	0.030
J1033.4+5252	2MASX J10331570+5252182	158.31548	52.87164	0.14036	24.3 ^{+0.3} _{–0.2}	2.35 ^{+0.24} _{–0.30}	24	XMM	0830500301	2018 Jun 2	80.7	0.006
								<i>NuSTAR</i>	60468003002	2018 Jun 2	61.0	0.012

Note. Column (1): ID from the Palermo BAT 100 months Catalog (Marchesi et al. 2019). (2): Source name. (3) and (4): R.A. and decl. (J2000 Epoch). (5): Redshift. (6): LOS column density from the joint *Swift*-XRT–*Swift*-BAT spectral fitting. (7): Photon index from the joint *Swift*-XRT–*Swift*-BAT spectral fitting. (8): Net counts in the 0.5–10 keV archival *Swift*-XRT spectrum. (9): Telescope used in the analysis. (10): Observation ID. (11): Observation date. (12): Total exposure, in ks. For *XMM-Newton* and *NuSTAR*, this is the sum of the exposures of each camera. (13): Average count rate (in cts s⁻¹), weighted by the exposure for *XMM-Newton* and *NuSTAR*, where observations from multiple instruments are combined. Count rates are computed in the 3–70 keV band for *NuSTAR* and in the 2–10 keV band otherwise.

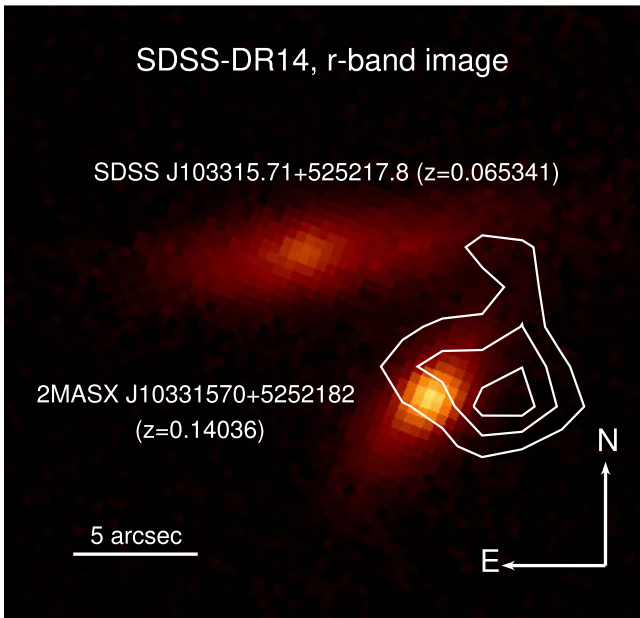


Figure 1. SDSS-DR14 r -band image at the position of 4BPCJ1033.4+5252, with the 0.5–10 keV *XMM-Newton* pn confidence contours overlapped. As can be seen, the X-ray emission is originated by the southern source, 2MASX J10331570+5252182. As a reference, the 4BPC source 95% confidence position uncertainty is $r = 3.1$.

The MYTORUS model is divided in three distinct components, to study the properties of an obscured AGN in a self-consistent way. The first one is a multiplicative component and is applied to the main power-law continuum: it describes the photoelectric absorption and Compton scattering attenuation, and allows one to measure the neutral hydrogen equatorial column density ($N_{\text{H,eq}}$). The second component is defined as the “reprocessed component,” or scattered continuum, and models the photons that reach the observer after one or more interactions with the obscuring material nearby the accreting SMBH. We refer to the normalization of the reprocessed component with respect to the main continuum as A_S . The cutoff energy of this second component can vary in the range of $E_c = [160\text{--}500]$ keV. In this analysis, we fix the parameter to a typical value, $E_c = 500$ keV, because in none of the three sources analyzed in this work do we find a significant improvement in the fit when leaving E_c free to vary. Finally, the last component models the emission of the iron fluorescent lines commonly observed in heavily obscured AGNs, namely, the Fe $K\alpha$ line at 6.4 keV and the $K\beta$ line at 7.06 keV. The normalization of these lines with respect to the main continuum is here named A_L and is tied to A_S , as both components are expected to have the same origin.

In XSPEC the fit to a spectrum with MYTORUS is described as follows:

$$\begin{aligned} \text{Model}_{\text{MYT}} = & \text{constant}_1 * \text{phabs} * \\ & (\text{mytorus_Ezero_v00.fits} * \text{pow}_1 \\ & + A_S * \text{mytorus_scatteredH500_v00.fits} \\ & + A_L * \text{mytl_V000010nEp000H500_v00.fits} \\ & + \text{constant}_2 * \text{pow}_2 + \text{mekal}), \end{aligned} \quad (1)$$

where constant_1 is the cross-normalization constant C_{InS} between the *XMM-Newton* and the *NuSTAR* data, phabs is

the Galactic absorption, the table *mytorus_Ezero_v00.fits* models the absorption to the zeroth-order continuum, *pow*₁, *mytorus_scatteredH500_v00.fits* accounts for the reprocessed continuum, *mytl_V000010nEp000H500_v00.fits* models the iron $K\alpha$ and $K\beta$ lines, and *constant*₂ accounts for the fraction of emission scattered, rather than absorbed by the obscuring torus (the photon index of this second power-law component, *pow*₂, is fixed to the one of *pow*₁). Finally, in 2MASX J10331570+5252182 we add to the model a phenomenological mekal component (Mewe et al. 1985) to account for the soft excess observed below 1 keV.

In its standard, “coupled” configuration, the column density of the reprocessed emission component is tied to the one associated to the zeroth-order continuum, and θ_{obs} is left free to vary. “MYTORUS decoupled” (Yaqoob 2012), instead, allows one to separate the LOS column density, $N_{\text{H,LOS}}$, from the reprocessed component column density, $N_{\text{H,S}}$, which can also be treated as a measurement of the torus average column density, because the reprocessed emission is given by photons scattered into the observer LOS from all possible directions. In “MYTORUS decoupled,” the viewing angle of the zeroth-order continuum absorber is fixed to $\theta_{\text{obs}} = 90^\circ$, so that $N_{\text{H,eq}} = N_{\text{H,LOS}}$; the viewing angle for the reprocessed component can instead be either $\theta_{\text{obs,AS,AL}} = 90^\circ$ (depicting a scenario where most of the reprocessed emission comes from material located between the observer and the accreting SMBH) or $\theta_{\text{obs,AS,AL}} = 0^\circ$ (where most of the reprocessed emission comes from the back side of the torus). In all the three sources studied in this work, we find that the $\theta_{\text{obs,AS,AL}} = 90^\circ$ scenario is preferred by the data.

3.2. borus02

The borus02 (Baloković et al. 2018) radiative transfer code models the reprocessed emission component of an AGN X-ray spectrum, i.e., following the MYTORUS nomenclature we introduced in the previous section, the “reprocessed component” and the neutral Fe emission lines. The obscuring material geometry in borus02 is quasi-toroidal, with conical polar cutouts. The torus covering factor, f_c , is a free parameter of the model and can vary in the range $f_c = [0.1\text{--}1]$. The angle between the torus axis and the observer can also vary, but we fix it to $\theta_{\text{obs}} = 87^\circ$, i.e., the upper boundary of the parameter in the model, corresponding to an almost “edge-on” configuration, to reduce potential degeneracies between this parameter and f_c .⁸

Another free parameter in borus02 is the average torus column density ($N_{\text{H,tor}}$). In this work, to find the best-fit $N_{\text{H,tor}}$ we follow the approach adopted by Baloković et al. (2018) when fitting single-epoch *NuSTAR* observations. We thus fit each of our spectra 36 times, each time fixing $N_{\text{H,tor}}$ to a different value in the range $\text{Log}(N_{\text{H,tor}}) = [22\text{--}25.5]$ (i.e., the lower and upper boundaries of the parameter in borus02); in each iteration, we increase the $\text{Log}(N_{\text{H,tor}})$ value by 0.1. The best-fit $N_{\text{H,tor}}$ is then the one corresponding to the fit having the minimum χ^2 . The best-fit f_c is then the one obtained at this $N_{\text{H,tor}}$.

⁸ We point out, however, that we are working on a paper on θ_{obs} and its possible trends with other spectral parameters (X. Zhao et al. 2019, in preparation), and we find that leaving θ_{obs} free to vary does not significantly affect the measurement of the other parameters.

The XSPEC configuration of borus02 is:

$$\begin{aligned} Model_{bor} = & constant_1 * phabs * (borus02_v170323a.fits \\ & + zphabs * cabs * cutoffpl_1 + constant_2 * \\ & cutoffpl_2 + mekal), \end{aligned} \quad (2)$$

where *borus02_v170323a.fits* is an additive table that models the reprocessed components, i.e., both the reprocessed continuum and the fluorescent lines. Since borus02 does not model the LOS absorption, we describe it with the components *zphabs* × *cabs*, which properly treats Compton scattering losses out of the LOS: the free parameter associated to these two components is $N_{H,LOS}$, which is identical in *zphabs* and *cabs* and varies independently from $N_{H,tor}$; finally, *cutoffpl*₁ and *cutoffpl*₂ are two power-law components with high-energy cutoff at $E = 500$ keV, for consistency with MYTORUS. The other components in the model are the same used with MYTORUS.

4. Results

In Table 2 we report a summary of the best-fit parameters obtained using the models described in the previous section. In the next sections, we will describe in detail the results of the spectral analysis for each of the three objects in our sample.

4.1. ESO 244–IG 030

We first fit the ESO 244–IG 030 joint *NuSTAR–XMM–Newton* spectrum using MYTORUS in its “coupled” configuration, obtaining a good best-fit statistic ($\chi^2/\text{d.o.f.} = 104.4/97$). We measure a photon index best-fit $\Gamma = 1.86^{+0.16}_{-0.17}$, a value close to the typical AGN one and harder than the one reported in Ricci et al. (2015) using the *Swift–XRT* and *Swift–BAT* data alone ($\Gamma = 2.45^{+0.35}_{-0.40}$). We also measure a significantly different LOS column density measurement; based on the joint *NuSTAR–XMM–Newton* fit, ESO 244–IG 030 is only mildly obscured, having $\text{Log}(N_{H,LOS}) = 22.75^{+0.08}_{-0.08}$.

To confirm the result obtained using MYTORUS coupled, we refit our data using MYTORUS in its “decoupled” configuration, allowing the column density of the reprocessed component ($N_{H,S}$) to vary independently from the the LOS column density. We find that the two models are statistically identical ($\chi^2/\text{d.o.f.} = 104.4/97$ for MYTORUS coupled and $\chi^2/\text{d.o.f.} = 104.2/97$ for MYTORUS decoupled) and all the free parameters measurements are in excellent agreement. Since the contribution of the reprocessed component is negligible, as expected for sources with low obscuration, $N_{H,S}$ is unconstrained. We report the best-fit MYTORUS decoupled model in Figure 2, top left panel.

Finally, we fit the ESO 244–IG 030 spectrum using borus02 (Figure 2, top right panel). Once again, the best-fit model is statistically identical to the other two ($\chi^2/\text{d.o.f.} = 104.2/97$) and all the main fit parameters are in agreement with those computed using MYTORUS in either configuration. Following the approach described in Section 3.2, we find that the best-fit average torus column density is $\text{Log}(N_{H,tor}) = 22.2$. We show the spectrum and best-fit model in Figure 2, top right panel. The best-fit covering factor corresponding to this $N_{H,tor}$ is $f_c = 1.00$, but the parameter is basically unconstrained. In fact, fixing the covering factor to $f_c = 0.1$ (i.e., the parameter

Table 2
Best-fits Results for the Joint *NuSTAR–XMM–Newton* Spectral Fitting of the Three Objects in Our Sample

Source	ESO 244 –IG 030	ESO 317–G 041	2MASX J10331570 +5252182
	MYTORUS coupled		
$\chi^2/\text{d.o.f.}$	104.4/97	118.4/122	128.8/114
C_{ins}	$1.41^{+0.17}_{-0.16}$	$1.61^{+0.35}_{-0.27}$	$1.22^{+0.13}_{-0.09}$
z	0.0256^f	0.0193^f	0.14036^f
Γ	$1.86^{+0.17}_{-0.16}$	$1.47^{+0.25}_{-0.07}$	1.40^f
Norm 10^{-4}	$2.34^{+0.87}_{-0.62}$	$4.39^{+6.42}_{-1.44}$	$1.73^{+0.80}_{-0.51}$
θ_{obs}	90^f	90^f	$61.0^{+4.0}_{-0.7}$
$\text{Log}(N_{H,eq})$	$22.75^{+0.08}_{-0.08}$	$23.88^{+0.08}_{-0.05}$	$24.30^{+0.16}_{-0.27}$
$\text{Log}(N_{H,LOS})$	$22.75^{+0.08}_{-0.08}$	$23.88^{+0.08}_{-0.05}$	$23.69^{+0.16}_{-0.27}$
A_S	1.00^f	$0.93^{+0.89}_{-0.59}$	$1.66^{+1.03}_{-0.78}$
$f_s 10^{-2}$	$4.9^{+1.8}_{-1.3}$...	$1.7^{+0.5}_{-0.3}$
kT	$0.28^{+0.23}_{-0.10}$
F_{2-10}	$4.63^{+0.27}_{-0.45}$	$2.47^{+0.28}_{-1.83}$	$2.92^{+12.57}_{-0.23}$
F_{15-55}	$10.12^{+1.72}_{-2.41}$	$62.58^{+1.46}_{-46.76}$	$38.80^{+15.88}_{-6.70}$
$\text{Log}(L_{2-10})$	$42.00^{+0.08}_{-0.10}$	$42.42^{+0.19}_{-0.34}$	$43.74^{+0.23}_{-0.09}$
$\text{Log}(L_{15-55})$	$42.02^{+0.34}_{-0.51}$	$42.68^{+0.29}_{-0.43}$	$44.43^{+0.27}_{-0.80}$
	MYTORUS decoupled “edge-on”		
$\chi^2/\text{d.o.f.}$	104.2/97	117.9/121	126.6/114
C_{ins}	$1.41^{+0.17}_{-0.16}$	$1.64^{+0.36}_{-0.28}$	$1.18^{+0.18}_{-0.16}$
Γ	$1.86^{+0.17}_{-0.16}$	$1.60^{+0.34}_{-0.20}$	1.40^f
norm 10^{-4}	$2.13^{+0.82}_{-0.57}$	$5.39^{+11.68}_{-2.98}$	$3.19^{+0.99}_{-0.75}$
A_S	1.00^f	$1.75^{+3.15}_{-0.70}$	$1.99^{+0.85}_{-0.70}$
$\text{Log}(N_{H,LOS})$	$22.76^{+0.07}_{-0.08}$	$23.86^{+0.21}_{-0.11}$	$23.89^{+0.08}_{-0.07}$
$\text{Log}(N_{H,S})$...	$24.14^{+0.31}_{-0.28}$	$23.05^{+0.24}_{-0.35}$
$f_s 10^{-2}$	$4.7^{+1.8}_{-1.3}$...	$0.9^{+0.4}_{-0.3}$
F_{2-10}	$4.71^{+0.66}_{-0.84}$	$2.44^{+0.27}_{-1.82}$	$3.00^{+0.24}_{-0.36}$
F_{15-55}	$10.14^{+2.69}_{-2.89}$	$61.47^{+2.78}_{-46.93}$	$37.25^{+2.96}_{-4.14}$
$\text{Log}(L_{2-10})$	$42.00^{+0.07}_{-0.09}$	$42.40^{+0.24}_{-0.49}$	$44.01^{+0.07}_{-0.09}$
$\text{Log}(L_{15-55})$	$42.01^{+0.34}_{-0.53}$	$42.64^{+0.37}_{-0.52}$	$44.74^{+0.26}_{-0.71}$
$\text{Log}(L_{bol})$	$43.00^{+0.08}_{-0.10}$	$43.38^{+0.25}_{-0.49}$	$45.16^{+0.10}_{-0.12}$
	borus02		
$\chi^2/\text{d.o.f.}$	104.2/97	117.8/122	124.6/114
C_{ins}	$1.41^{+0.17}_{-0.15}$	$1.64^{+0.37}_{-0.27}$	$1.16^{+0.13}_{-0.13}$
Γ	$1.85^{+0.17}_{-0.17}$	$1.56^{+0.20}_{-0.16}$	1.40^f
norm 10^{-4}	$2.10^{+0.85}_{-0.58}$	$4.87^{+5.06}_{-1.96}$	$3.98^{+1.28}_{-0.86}$
$\text{Log}(N_{H,LOS})$	$22.77^{+0.07}_{-0.09}$	$23.85^{+0.08}_{-0.10}$	$24.07^{+0.12}_{-0.14}$
$\text{Log}(N_{H,tor})$	22.2^f	24.1^f	23.4^f
Z/Z_{\odot}	1.00^f	1.00^f	$0.35^{+0.16}_{-0.15}$
f_c	1.00^f	$0.58^{+0.42}_{-0.30}$	$0.90^{+0.10}_{-0.24}$
$f_s 10^{-2}$	$4.7^{+1.7}_{-1.3}$...	$0.8^{+0.3}_{-0.3}$
F_{2-10}	$4.71^{+0.25}_{-0.46}$	$2.44^{+0.27}_{-1.08}$	$3.01^{+0.32}_{-0.78}$
F_{15-55}	$9.79^{+1.54}_{-2.16}$	$61.73^{+2.50}_{-29.01}$	$38.61^{+2.82}_{-8.66}$
$\text{Log}(L_{2-10})$	$42.00^{+0.07}_{-0.09}$	$42.36^{+0.34}_{-0.39}$	$44.11^{+0.08}_{-0.09}$
$\text{Log}(L_{15-55})$	$42.01^{+0.35}_{-0.49}$	$42.60^{+0.32}_{-0.45}$	$44.86^{+0.28}_{-1.11}$

Note. $C_{ins} = C_{NuS/XMM}$ is the cross calibration between *NuSTAR* and *XMM–Newton*, z is the source redshift, Γ is the power-law photon index, norm is the main power-law normalization at 1 keV, in units of photons $\text{s}^{-1} \text{cm}^{-2} \text{keV}^{-1}$, $N_{H,eq}$ is the equatorial column density, in units of cm^{-2} , θ_{obs} is the inclination angle between the observer LOS and the torus axis (in degrees), A_S is the intensity of the reprocessed component, f_s is the fraction of emission scattered, rather than absorbed by the obscuring torus, and kT is the temperature (in keV) of the phenomenological *mekal* component used to fit the excess at <1 keV. $N_{H,LOS}$ is the LOS column density, while $N_{H,S}$ and $N_{H,tor}$ are the average torus column densities as measured using MYTORUS decoupled and borus02, respectively, and f_c is the torus covering factor, $f_c = \cos(\theta_{tor})$; Z is the metallicity of the borus02 component. Finally, F_{2-10} and F_{15-55} are the observed fluxes (in units of $10^{-13} \text{erg cm}^{-2} \text{s}^{-1}$) in the 2–10 and 15–55 keV bands, while L_{2-10} and L_{15-55} are the intrinsic luminosities (in units of erg s^{-1}) in the same bands, and L_{bol} is the bolometric luminosity (in units of erg s^{-1}) derived using L_{2-10} and the bolometric correction for type 2 AGN derived by Lusso et al. (2012).

lower limit) we obtain a best-fit statistic $\chi^2/\text{d.o.f.} = 104.4/97$, with a statistic variation $\Delta\chi^2 = 0.2$. Once again, this is not an unexpected result, since according to our model the contribution of the reprocessed component to the 2–70 keV emission is negligible.

In conclusion, we find that ESO 244–IG 030 is not a CT-AGN, and is in fact only moderately obscured, fully supporting our original assumption (i.e., that in sources with only low-quality 2–10 keV and *Swift*-BAT data and soft best-fit photon index the LOS column density is likely overestimated).

4.2. ESO 317-IG 030

Due to the low quality of the *XMM-Newton* data below 3 keV, which resulted in an artificial underestimation of the photon index Γ , we decided to fit the spectrum of ESO 317-IG 030 in the 3–70 keV energy range.

Following the same approach described in the previous section, we first fit the joint *NuSTAR*–*XMM-Newton* spectrum using *MYTORUS* in its “coupled” configuration: this first model leads to an excellent fit statistic ($\chi^2/\text{d.o.f.} = 118.4/122$). The photon index best-fit value we obtain is significantly harder than the one measured using the *Swift*-XRT and *Swift*-BAT data ($\Gamma_{\text{XRT-BAT}} = 2.20^{+0.27}_{-0.22}$), i.e., $\Gamma_{\text{XMM-NuS}} = 1.47^{+0.25}_{-0.07}$. Similarly to what we observed in ESO 244–IG 030, this change implies a significant variation in the LOS column density measured with *NuSTAR* and *XMM-Newton* with respect to the one derived from the *Swift*-XRT and *Swift*-BAT data: indeed, we find that $N_{\text{H,LOS,XMM-NuS}}$ is three times smaller than $N_{\text{H,LOS,XRT-BAT}}$ and ESO 317-IG 030 is consequently reclassified as a Compton thin AGN, having $\text{Log}(N_{\text{H,LOS}}) = 23.88^{+0.08}_{-0.05}$.

We then refit the data with *MYTORUS* in its decoupled configuration. We show the best-fit model in Figure 2, central left panel. The best-fit statistic is equivalent to the one of *MYTORUS* coupled ($\chi^2/\text{d.o.f.} = 117.9/121$). Similarly, the best-fit parameters are also in close agreement with those obtained using “*MYTORUS* coupled,” the best-fit photon index being $\Gamma = 1.60^{+0.34}_{-0.20}$ and the LOS column density being $\text{Log}(N_{\text{H,LOS}}) = 23.86^{+0.21}_{-0.11}$. We also find that the obscuring torus is likely to be homogenous, since the column density responsible for the scattered emission (which can be treated as the torus average column density) is $\text{Log}(N_{\text{H,S}}) = 24.14^{+0.31}_{-0.28}$, in good agreement with the LOS one.

We complete our spectral analysis using *borus02*, and even in this case, the fit statistic is fully consistent with those of the two *MYTORUS* fits ($\chi^2/\text{d.o.f.} = 117.8/122$). The best-fit parameters are also in excellent agreement with the *MYTORUS* ones: the photon index is $\Gamma = 1.56^{+0.20}_{-0.16}$, the LOS column density is $\text{Log}(N_{\text{H,LOS}}) = 23.85^{+0.08}_{-0.10}$ and the torus average column density for which we obtain the smallest χ^2 is $\text{Log}(N_{\text{H,tor}}) = 24.1$. Since ESO 317-IG 030 is significantly more obscured than ESO 244–IG 030, we are also able to put some (albeit loose) constraints on the torus covering factor, $f_c = 0.58^{+0.42}_{-0.30}$. We note that in *MYTORUS* coupled the torus covering factor is also assumed to be $f_c = 0.50$. The best-fit model is shown in Figure 2, central right panel.

In summary, the fit of the *NuSTAR* and *XMM-Newton* data depicts a scenario where ESO 317-IG 030 has a harder spectrum and is significantly less obscured than it was measured using the low-quality *Swift*-XRT and *Swift*-BAT data. Based on our new measurements, ESO 317-IG 030 is reclassified as a Compton thin AGN, although the 90%–95%

(depending on the model) upper boundary of the LOS column density is above the $\text{Log}(N_{\text{H,LOS}}) = 24$ threshold.

4.3. 2MASX J10331570+5252182

Before performing our spectral analysis, we check if the assumptions on the source counterpart and redshift reassociation reported in Section 2 are correct. To do so, we fit our data leaving z as a free parameter. Thanks to the high spectral quality of the *XMM-Newton* and *NuSTAR* data, we are able to tightly constrain z . With all three models used in our analysis, we find a redshift value in excellent agreement with $z_{\text{spec}} = 0.14036$, i.e., the spectroscopic redshift measured for 2MASX J10331570+5252182. More in detail, when using *MYTORUS* in its “coupled” configuration we obtain $z_{\text{MyTC}} = 0.147^{+0.008}_{-0.012}$, with *MYTORUS* in “decoupled” mode we measure a redshift $z_{\text{MyTC}} = 0.145^{+0.010}_{-0.007}$, and with *borus02* we find $z_{\text{bor}} = 0.147^{+0.008}_{-0.009}$. We also point out that using the previous redshift value ($z = 0.0653$) significantly affects the fit statistic, with a variation in χ^2 $\Delta\chi^2 \sim 40$, regardless of the adopted model. For these reasons, in the rest of the analysis we fix the source redshift to $z_{\text{spec}} = 0.14036$.

As for the previous two objects, we first fit the X-ray spectrum using “*MYTORUS* coupled”; the best-fit statistic we obtain is good, being $\chi^2/\text{d.o.f.} = 128.8/114$. We find that the photon index is pegged at the parameter lower boundary, $\Gamma = 1.4$, i.e., that the source is particularly hard. Such a hard photon index may be unphysical (the typical AGN photon index is $\Gamma = 1.7$ – 1.9 , see, e.g., Marchesi et al. 2016) and could imply that the LOS column density measurement we obtain is underestimated. While in ESO 244–IG 030 and ESO 317-IG 030 the fit is insensitive to θ_{obs} , which we thus fixed to $\theta_{\text{obs}} = 90^\circ$, in 2MASX J10331570+5252182 the fit is significantly improved by allowing the angle between the observer and the torus axis, θ_{obs} , to vary. Particularly, the best-fit solution is $\theta_{\text{obs}} = 61.0^{+4.0}_{-0.7}$, i.e., the source would be observed at the edge of the torus, whose opening angle is $\theta_{\text{OA}} = 60^\circ$. This is a scenario commonly observed when using “*MYTORUS* coupled” (see, e.g., Zhao et al. 2019a, 2019b), but is also physically unlikely, since the chance of observing the accreting SMBH exactly at the edge of the obscuring torus is small. The equatorial column density we measure is $N_{\text{H,eq}} = 2.29^{+1.07}_{-0.93} \times 10^{24} \text{ cm}^{-2}$, and the corresponding LOS column density is therefore $N_{\text{H,LOS}} = N_{\text{H,eq}} [1 - 4 \cos^2 \theta_{\text{obs}}]^{1/2} = 4.89^{+2.62}_{-2.27} \times 10^{23} \text{ cm}^{-2}$.

When fitting the 2MASX J10331570+5252182 0.6–50 keV spectrum with “*MYTORUS* decoupled” we again find that the photon index is pegged to the parameter lower boundary, $\Gamma = 1.4$. The LOS column density is slightly higher, although consistent within the 90% confidence uncertainties, than the one measured using “*MYTORUS* coupled,” being $\text{Log}(N_{\text{H,LOS,MyTD}}) = 23.89^{+0.08}_{-0.07}$. Interestingly, the column density linked to the reprocessed emission is found to be significantly smaller ($\text{Log}(N_{\text{H,S}}) = 23.05^{+0.24}_{-0.35}$), potentially hinting to a scenario where the accreting SMBH is observed through an overdensity in a patchy torus. We show the best-fit “*MYTORUS* decoupled” model in Figure 2, bottom left panel.

Finally, we find that using *borus02* the fit statistic is significantly improved when allowing the metallicity of the *borus02* model to vary with respect to the solar value; the best-fit metallicity is $Z/Z_\odot = 0.35^{+0.16}_{-0.15}$. The other parameters are in good agreement with those measured using “*MYTORUS* decoupled”: the photon index is pegged at $\Gamma = 1.4$ and the

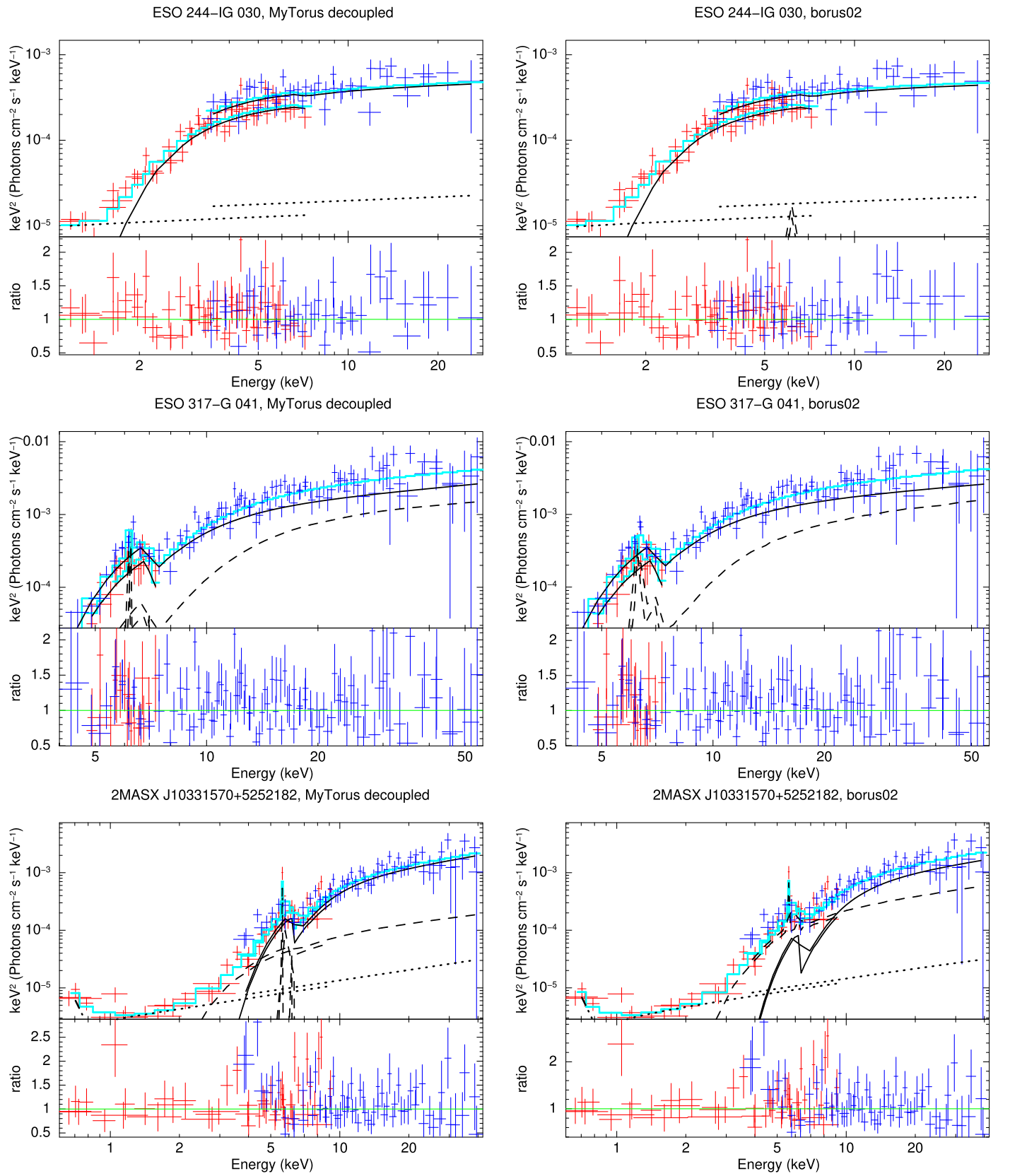


Figure 2. Background-subtracted spectra (top panel) and data-to-model ratio (bottom) of the three sources in this work. *XMM-Newton* data are plotted in red, *NuSTAR* data in blue. In the left column we report the best-fit models obtained using *MYtorus* in “decoupled” configuration, while in the right column we show the *borus02* best-fit models. The best-fitting model is plotted as a cyan solid line, the main emission component is plotted as a black solid line, the reprocessed component is plotted as a black dashed line and the main power-law component scattered, rather than absorbed, by the torus is plotted as a black dotted line. Finally, the phenomenological *mekal* component used to model the excess below 1 keV is plotted as a dashed-dotted black line.

LOS column density is just above the CT threshold ($\text{Log}(N_{\text{H,LOS}}) = 24.07^{+0.12}_{-0.14}$). The average torus column density is also in good agreement with the value obtained using “MYTorus decoupled,” being $\text{Log}(N_{\text{H,tor}}) = 23.4$. All three models have similar fit statistic, but we favor the “MYTorus decoupled” and *borus02* solutions given the low physical likelihood of the scenario depicted by “MYTorus coupled.” The best-fit model is shown in Figure 2, bottom right panel.

Interestingly, we find a second possible best-fit model for 2MASX J10331570+5252182 using *borus02*. In this second scenario (whose fit statistic is $\chi^2/\text{d.o.f.} = 124.9/144$, with a difference in $\chi^2 \Delta\chi^2 = 0.3$ with respect to the first solution), the accreting SMBH is buried in a heavily CT torus with $\text{Log}(N_{\text{H,tor}}) = 25$ and $\text{Log}(N_{\text{H,LOS}}) = 25.05^{+0.95}_{-0.13}$. The best-fit photon index is $\Gamma = 1.90^{+0.19}_{-0.14}$ and the torus covering factor is pegged at the parameter lower boundary, $f_c = 0.1$. While these parameters are all physically plausible, the intrinsic luminosity associated to the source is extremely high, being $\text{Log}(L_{2-10}) > 46$, i.e., almost an order of magnitude higher than the luminosities observed in luminous quasars. For this reason, we rule out this high-luminosity solution, which nonetheless confirms that 2MASX J10331570+5252182 must be heavily obscured.

We also point out that, although in our best-fit solution the LOS column density is below the CT threshold, the fact that the photon index is pegged at $\Gamma = 1.4$ suggests that we might be underestimating $N_{\text{H,LOS}}$, and 2MASX J10331570+5252182 could be a CT-AGN. As a test, we refit our spectrum fixing the photon index to a typical AGN value, $\Gamma = 1.8$. In all three models, the variation in χ^2 with respect to the best-fit model with $\Gamma = 1.4$ is $\Delta\chi^2 \sim 11.5$ and the reduced χ^2 is $\chi^2_\nu \sim 1.19$: the $\Gamma = 1.8$ is therefore statistically plausible, although less likely than the $\Gamma = 1.4$ one.

When fixing the photon index to $\Gamma = 1.8$, we find a 30%–35% increase in $N_{\text{H,LOS}}$ and a corresponding increase in the main power-law normalization by a factor of ~ 4 , regardless of the adopted model. For all the other parameters the best-fit values are consistent, within the uncertainties, with those obtained using $\Gamma = 1.4$. Using “MYTorus decoupled” and “*borus02*,” the increase in LOS column density shifts the parameter best-fit value above the CT threshold, $\text{Log}(N_{\text{H,LOS}}) > 24$.

In conclusion, all the models used in our analysis are statistically acceptable and they all depict a heavily obscured, likely CT scenario for 2MASX J10331570+5252182. This makes this source fairly unique among those in the 100 months BAT catalog, since *Swift*-BAT is biased against obscured AGN: for example, Burlon et al. (2011) reported that in the 36 months BAT catalog no CT-AGNs were detected at redshifts $z > 0.04$; similarly, only 3 out of 55 candidate CT-AGNs in the 70 months BAT catalog have redshift $z > 0.1$ (Ricci et al. 2015), one of which (2MASXJ03561995–6251391) was reclassified as Compton thin in M18 and M19. We further discuss the potential uniqueness of 2MASX J10331570+5252182 in Section 5.3.

5. Discussion and Conclusions

5.1. The Key Role of NuSTAR in the Characterization of Heavily Obscured AGN

In M18 and M19 we showed how the addition of *NuSTAR* significantly improves the results of the X-ray spectral analysis

of heavily obscured AGNs. To check if this evidence is confirmed also in our new sample of object, we refit the *XMM-Newton* spectra alone.

ESO 244–IG 030 would have been found to be a non-CT AGN even using the *XMM-Newton* data alone. However, while the best-fit parameters measured with *XMM-Newton* are in good agreement with those derived using both *XMM-Newton* and *NuSTAR* ($\Gamma_{\text{XMM}} = 1.89^{+0.44}_{-0.39}$; $\text{Log}(N_{\text{H,LOS,XMM}}) = 22.78-0.13+0.11$), the uncertainties on the parameters are significantly higher: the Γ uncertainty increases by a factor ~ 2 , and we measure a $\sim 50\%$ increase in the $N_{\text{H,LOS}}$ uncertainty. Finally, as expected, the source covering factor is unconstrained.

ESO 317–G 041 is the source in our sample where the lack of *NuSTAR* data would affect the fit reliability the most, since the source *XMM-Newton* count statistic in the 3–10 keV band is fairly poor (~ 300 counts overall). The photon index is pegged to the model lower boundary ($\Gamma = 1.4$), while the uncertainties on $N_{\text{H,LOS}}$ are a factor ~ 2.5 larger than those computed using the joint *NuSTAR* and *XMM-Newton* spectra. Finally, no constrain can be put on both the torus average column density and on the covering factor based on the *XMM-Newton* data only.

Finally, for 2MASX J10331570+5252182 the “*XMM-Newton*-only” best-fit results are once again in good agreement with the joint *XMM-Newton* and *NuSTAR* ones ($\Gamma_{\text{XMM}} = 1.4$ and $\text{Log}(N_{\text{H,LOS,XMM}}) = 24.15^{+0.20}_{-0.19}$), but the uncertainties on $N_{\text{H,LOS,XMM}}$ are $\sim 40\%$ larger. Furthermore, without the *NuSTAR* data f_c and $N_{\text{H,tor}}$ are fully unconstrained.

Summarizing, while the *XMM-Newton* data alone would have allowed one to reliably measure the main spectral parameters (Γ and $N_{\text{H,LOS}}$), the parameter uncertainties would have been significantly larger, thus limiting the significance of the fit results. Furthermore, the lack of *NuSTAR* would have prevented one to measure other important parameters, particularly the torus covering factor and average column density.

5.2. Measurements of the Iron $K\alpha$ Line Equivalent Width

Historically, candidate heavily obscured AGNs have been selected in the X-rays based on the presence of a prominent iron $K\alpha$ line at 6.4 keV, having equivalent width (EW) $\gtrsim 1$ keV: however, the low spectral quality of the *Swift*-XRT data for the three sources in our sample did not allow us to constrain the line EW, a goal now achievable using the *NuSTAR* and *XMM-Newton* data. To do so, since neither MYTorus nor *borus02* allow one to use the task *eqwidth* in XSPEC, we follow the approach described in Yaqoob et al. (2015) to compute the Iron line EW using MYTorus. We thus first compute the continuum flux at 6.4 keV, without including the contribution of the emission line. Then, we measure the flux of the iron line in the energy range $E = [0.95 E_{K\alpha} - 1.05 E_{K\alpha}]$ (i.e., between 6.08 and 6.72 keV, rest frame). The line EW is then obtained by multiplying by $(1+z)$ the ratio between the line flux and the continuum flux at 6.4 keV.

As reported in Section 4.1, ESO 244–IG 030 is only moderately obscured, having $\text{Log}(N_{\text{H,LOS}}) \leq 22.8$. Consequently, this source does not have a prominent iron line, and in fact no clear emission feature is observed at $E \sim 6.4$ keV. The upper limit on the line EW is $\text{EW}_{K\alpha, \text{MyTC}} \leq 0.05$ keV and $\text{EW}_{K\alpha, \text{MyTD}} \leq 0.09$ keV using either “MYTorus coupled” or “decoupled,” respectively.

ESO 317–G 041 is significantly more obscured than ESO 244–IG 030, having $\text{Log}(N_{\text{H,LOS}}) \sim 23.85$, and an emission feature is visible in its spectrum at ~ 6.4 keV. The EW of the line is, however, slightly smaller than the values typically observed in CT-AGNs, being $\text{EW}_{K\alpha, \text{MyTC}} = 0.21_{-0.19}^{+0.03}$ keV using “MYTorus coupled and $\text{EW}_{K\alpha, \text{MyTC}} < 0.27$ keV with “MYTorus decoupled.”

As can be seen, the iron $K\alpha$ EW measurements further confirm that both ESO 244–IG 030 and ESO 317–G 041 have significantly lower LOS column density than was expected based on the *Swift*-XRT and *Swift*-BAT spectral fitting.

Finally, 2MASX J10331570+5252182 is the source in our sample where the iron line is most clearly visible in the spectrum and, consequently, the source where the line EW is the largest; with “MYTorus coupled” (“decoupled”) we measure $\text{EW}_{K\alpha, \text{MyTC}} = 0.34 \pm 0.07$ keV ($\text{EW}_{K\alpha, \text{MyTD}} = 0.30_{-0.12}^{+0.11}$ keV). We also compute EW using the best-fit models obtained fixing the photon index to $\Gamma = 1.8$, and the results are in good agreement with those obtained using the $\Gamma = 1.4$ fits, being $\text{EW}_{K\alpha, \text{MyTC}, \Gamma=1.8} = 0.39_{-0.18}^{+0.09}$ keV and $\text{EW}_{K\alpha, \text{MyTD}, \Gamma=1.8} = 0.21_{-0.05}^{+0.20}$ keV.

5.3. Intrinsic X-Ray and Bolometric Luminosity, and the SMBH Mass

In Table 2 we report the intrinsic, absorption-corrected luminosities of the three sources in our sample in the 2–10 keV and 15–55 keV bands. For all sources, all the three models used in our analysis produce luminosities values that are in agreement within the 90% uncertainties.

Both ESO 244–IG 030 and ESO 317–G 041 are low/moderate luminosity AGNs: the first has $L_X \sim 10^{42}$ erg s^{−1} in both the 2–10 keV and in the 15–55 keV band, while the latter has $L_{2-10} \sim 2.5 \times 10^{42}$ erg s^{−1} and $L_{15-55} \sim 4.5 \times 10^{42}$ erg s^{−1}. While 2MASX J10331570+5252182 is far more distant than the other two sources in our sample ($z = 0.14036$ versus $z \sim 0.019$ – 0.026), all three objects have similar observed fluxes. Consequently, 2MASX J10331570+5252182 is significantly more luminous than the other two, and is in fact a candidate CT quasar, having $L_{2-10} \sim 10^{44}$ erg s^{−1} and $L_{15-55} \sim 7 \times 10^{44}$ erg s^{−1}. As we mentioned in Section 4.3, MASX J10331570+5252182 is one of the very few candidate CT-AGNs detected by *Swift*-BAT at $z > 0.1$. Its quasar-like luminosity is also uncommon in heavily obscured AGNs detected by *Swift*-BAT, since among the 35 100 months BAT-selected, candidate CT-AGNs studied in M18, M19, only two have $\text{Log}(L_{2-10}) > 44$ (namely, MASX J03561995–6251391 and MRK 3).

The intrinsic 2–10 keV luminosities we derived from our spectral fitting can be used to estimate the AGN bolometric luminosity (i.e., the total AGN emission integrated over the whole electromagnetic spectrum), using one of the several bolometric corrections reported in the literature (see, e.g., Elvis et al. 1994; Marconi et al. 2004; Lusso et al. 2012; Brightman et al. 2017). In this work, we use the bolometric correction for Type 2 AGN computed by Lusso et al. (2012, we use their “spectro+photo” sample parameters), and the 2–10 keV luminosities derived using the “MYTorus decoupled” model. The bolometric luminosities we obtain are $L_{\text{bol}} = 1.00_{-0.21}^{+0.20} \times 10^{43}$ erg s^{−1} for ESO 244–IG 030, $L_{\text{bol}} = 2.40_{-1.62}^{+1.87} \times 10^{43}$ erg s^{−1} for ESO 317–G 041, and $L_{\text{bol}} = 1.66_{-0.40}^{+0.43} \times 10^{45}$ erg s^{−1} for 2MASX J10331570+5252182.

Finally, we use the bolometric luminosities derived using the Lusso et al. (2012) corrections to get a rough estimate of the

masses of the accreting SMBHs powering the three AGNs in our sample. To do so, we assume an Eddington ratio $\lambda_{\text{Edd}} = L_{\text{bol}}/L_{\text{Edd}} = 0.1$ (a typical value for AGNs in the nearby universe, see, e.g., Marconi et al. 2004). In this equation, L_{Edd} is the Eddington luminosity, defined as

$$L_{\text{Edd}} = \frac{4\pi GM_{\text{BH}}m_p c}{\sigma_T}, \quad (3)$$

where M_{BH} is the SMBH mass and m_p is the mass of proton. The black hole mass is therefore

$$M_{\text{BH}} = \frac{L_{\text{bol}} \sigma_T}{4\pi Gm_p c \lambda_{\text{Edd}}}. \quad (4)$$

For the three objects in our sample, we estimate the following BH masses, in units of M_{\odot} : $\text{Log}(M_{\text{BH}}) = 5.90_{-0.10}^{+0.08}$ for ESO 244–IG 030; $\text{Log}(M_{\text{BH}}) = 6.28_{-0.49}^{+0.25}$ for ESO 317–G 041; and $\text{Log}(M_{\text{BH}}) = 8.12_{-0.12}^{+0.10}$ for 2MASX J10331570+5252182. The relatively low BH masses we derive for ESO 244–IG 030 and ESO 317–G 041, while not physically implausible (BH masses in AGNs usually vary in the range $\text{log}(M_{\text{BH}}/M_{\odot}) \sim 6.0$ – 9.8 ; see, e.g., Woo & Urry 2002), may indicate that the Eddington ratio in these sources is lower than $\lambda_{\text{Edd}} = 0.1$, i.e., the objects are undergoing a less efficient accretion phase.

5.4. Covering Factor

As mentioned in the previous sections, the *borus02* model allows one to constrain the geometry of the obscuring material surrounding the accreting SMBH, using as a free parameter the torus covering factor, f_c . We were not able to put any significant constraint on f_c in ESO 244–IG 030, since the source is only moderately obscured and the contribution to the total emission of the reprocessed component modeled by *borus02* is negligible. We are instead able to measure the torus covering factor for the other two sources in our sample: ESO 317–G 041 has $f_c = 0.58_{-0.30}^{+0.42}$, close to the value adopted by MYTorus ($f_c = 0.5$) and predicted by the so-called “unified model” for AGNs 2MASX J10331570+5252182, instead, favors a high covering factor solution, $f_c = 0.90_{-0.24}^{+0.10}$.

To give a better sense of how well f_c and $N_{\text{H,tor}}$ are constrained in each source, in Figure 3 we report how both f_c and the best-fit χ^2 vary as a function of the torus average covering factor. As can be seen, in ESO 244–IG 030 (left panel) the fit is insensitive to variations in $N_{\text{H,tor}}$ or f_c , and the difference in χ^2 between a fit with $\text{Log}(N_{\text{H,tor}}) = 22.2$ and $f_c = 1.0$ and one with $\text{Log}(N_{\text{H,tor}}) = 25.0$ and $f_c = 0.1$ is $\Delta\chi^2 < 1$. In ESO 317–G 041 (central panel) the covering factor is loosely constrained, since for the majority of average column density values (i.e., for $\text{Log}(N_{\text{H,tor}}) < 24.6$) we find that the best-fit f_c is $f_c < 0.6$. Finally, as already discussed in Section 4.3, there are two potential solutions for 2MASX J10331570+5252182 (right panel of Figure 3); the one we favor based on the physical reliability of the best-fit parameters is the high- f_c one, ($f_c = 0.90_{-0.24}^{+0.10}$ for an average torus column density $\text{Log}(N_{\text{H,tor}}) = 23.4$). The low- f_c solution ($f_c = 0.1$; $\text{Log}(N_{\text{H,tor}}) = 25$) instead, while statistically equivalent ($\Delta\chi^2 = 0.3$), is ruled out because of the extreme AGN luminosity ($\text{Log}(L_{2-10}) > 46$) implied by the model.

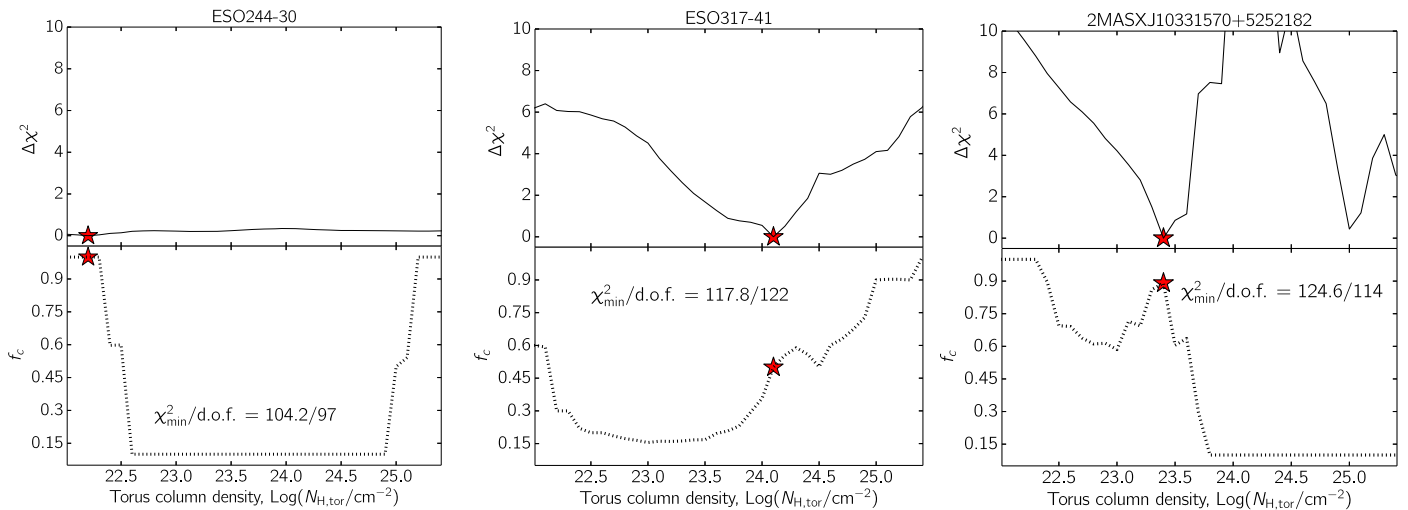


Figure 3. Estimate of the torus covering factor in ESO 244–IG 030 (left) and ESO 317–G 041 (center) and 2MASX J10331570+5252182. Top panel: difference between the best-fit, minimum χ^2 (χ^2_{\min}) and the χ^2 associated to $\log(N_{\text{H,tor}})$, as a function of the torus average column density. Bottom panel: torus covering factor as a function of the torus average column density. In both panels, we plot as a red star the combination of parameters associated to χ^2_{\min} .

5.5. Conclusions

We analyzed the joint *NuSTAR* and *XMM-Newton* spectrum of three candidate CT-AGNs selected in the 100 months BAT catalog: these objects were previously classified as CT-AGNs based on low-quality *Swift*-XRT and *Swift*-BAT data, and had soft ($\Gamma > 2.2$) photon indices that suggested a potential overestimation of the LOS column density ($N_{\text{H,LOS}}$). In all three sources, we found that both Γ and $N_{\text{H,LOS}}$ were indeed significantly overestimated. For two objects (ESO 244–IG 030 and ESO 317–G 041) this also implied a reclassification of the source from CT to Compton thin, thus confirming a trend already observed in previous works (Marchesi et al. 2018, 2019), which affects the local universe intrinsic CT fraction measurement and, consequently, the predictions of the AGN population synthesis models (e.g., Ananna et al. 2019).

Thanks to the good *XMM-Newton* spatial resolution and the excellent quality of the *NuSTAR* and *XMM-Newton* spectra, we find that the source 4BPCJ1033.4+5252 (i.e., source SWIFTJ1033.8+5257 in Ricci et al. 2015) was mistakenly associated to the galaxy SDSS J103315.71+525217.8 at $z = 0.0653$. The correct counterpart is instead 2MASX J10331570+5252182. This source redshift ($z = 0.14036$) makes it one of the most distant candidate CT-AGNs detected by *Swift*-BAT, and possibly even a rare CT quasar.

Finally, the high quality of the *NuSTAR* and *XMM-Newton* data allowed us to constrain several parameters that were previously unconstrained, particularly in the two more obscured objects, i.e., ESO 317–G 041 and 2MASX J10331570+5252182. We measured the iron $K\alpha$ EW, the torus covering factor and the average torus column density. We found that in ESO 317–G 041 the obscuring material is fairly uniformly distributed, while in 2MASX J10331570+5252182 the LOS column density is significantly higher than the torus average column density, which hints to a possible “patchy torus” scenario.

S.M., M.A., and X.Z. acknowledge funding under NASA contract 80NSSC17K0635 and 80NSSC19K0531. A.C. acknowledges support from the ASI/INAF grant I/037/12/0-011/13.

Appendix

Spectral Analysis of 2MASX J10313591–4206093, a Source Serendipitously Detected in the Field of View of ESO 317–G041

In this appendix we report the joint *NuSTAR*–*XMM-Newton* spectral analysis of 2MASX J10313591–4206093, which we detected in the field of view of ESO 317–G041 in both the *NuSTAR* and the *XMM-Newton* observation; 2MASX J10313591–4206093 is located at a distance of $\sim 205''^9$ from ESO 317–G041, and its redshift is $z = 0.06112$. In Table 3 we report the best-fit parameters obtained in our analysis.

Following the same approach used to analyze the three objects previously discussed in this work, we first fit the *NuSTAR*–*XMM-Newton* spectrum with MYTORUS used in its “coupled” configuration. The best-fit statistic is good ($\chi^2/\text{d.o.f.} = 147.5/144$), the source has a relatively hard best-fit photon index ($\Gamma = 1.49^{+0.16}_{-0.09}$) and is moderately obscured, having $\text{Log}(N_{\text{H,LOS}}) = 23.54^{+0.06}_{-0.06}$.

Using MYTORUS in its “decoupled configuration” (i.e., allowing the reprocessed component column density, $N_{\text{H,tor}}$, to vary independently from $N_{\text{H,LOS}}$) instead, leads to a slightly softer solution for the main power-law photon index ($\Gamma = 1.63^{+0.20}_{-0.23}$). The LOS column density is consistent with the one measured with “MYTORUS coupled,” being $\text{Log}(N_{\text{H,LOS}}) = 23.55^{+0.07}_{-0.06}$, while the column density responsible for the reprocessed emission is slightly higher ($N_{\text{H,tor}} = 23.97^{+0.45}_{-0.83}$), although consistent with the LOS one within the 90% confidence uncertainties. Finally, the fit statistic ($\chi^2/\text{d.o.f.} = 147.5/144$) is practically identical to the one obtained using MYTORUS in its coupled configuration. We report the *NuSTAR* and *XMM-Newton* spectra and the “MYTORUS decoupled” best-fit model in Figure 4, left panel.

Finally, the borus02 best-fit model has a better fit statistic than the two MYTORUS models ($\chi^2/\text{d.o.f.} = 141.8/144$; $\Delta\chi^2_{\text{MyT-bor}} = 5.7$). The main difference between the models is in the best-fit photon index, which is significantly softer

⁹ The 95% confidence error radius of 4BPC J1031.5–4203, the *Swift*-BAT source associated to ESO 317–G041, is $r = 119''$, thus we do not expect any significant contribution of 2MASX J10313591–4206093 to the 15–150 keV spectrum of 4BPC J1031.5–4203.

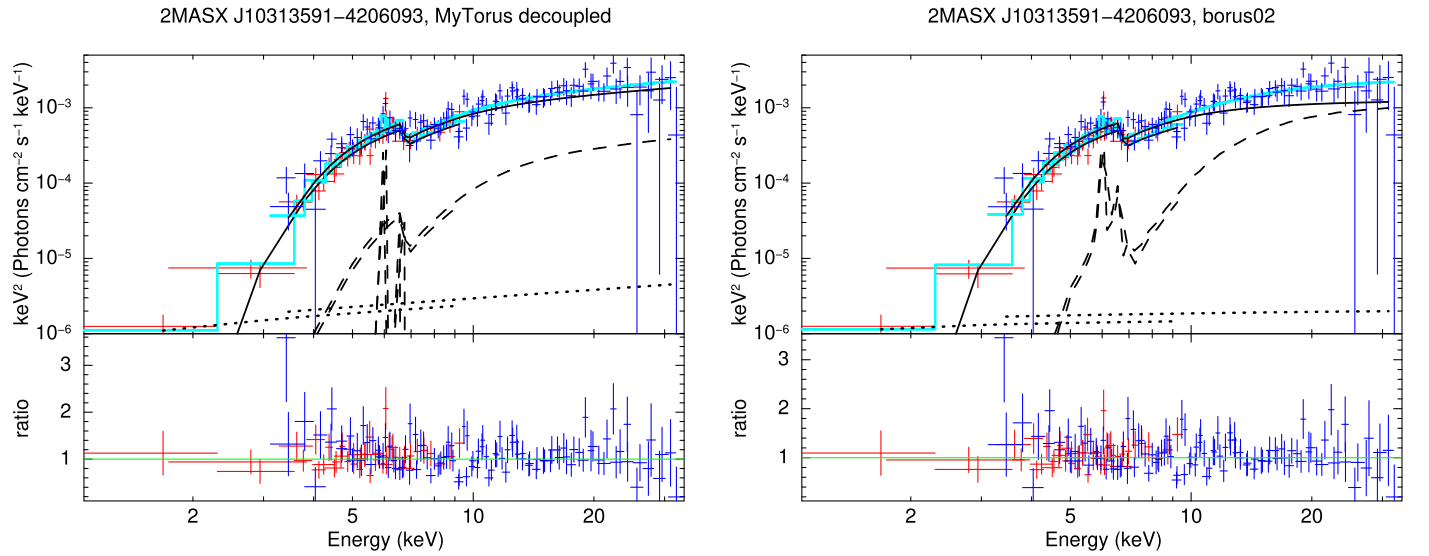


Figure 4. Background-subtracted spectra (top panel) and data-to-model ratio (bottom) of 2MASX J10313591–4206093. *XMM-Newton* data are plotted in red, *NuSTAR* data in blue. In the left column we report the best-fit models obtained using *MYTorus* in “decoupled” configuration, while in the right column we show the *borus02* best-fit models. The best-fitting model is plotted as a cyan solid line, the main emission component is plotted as a black solid line, the reprocessed component is plotted as a black dashed line and the main power-law component scattered, rather than absorbed, by the torus is plotted as a black dotted line.

Table 3

Best-fits Results for the Joint *NuSTAR*–*XMM-Newton* Spectral Fitting of 2MASX J10313591–4206093

	MYTorus Coupled	MYTorus Decoupled	borus02
$\chi^2/\text{d.o.f.}$	147.5/144	147.5/144	141.8/144
C_{Ins}	$1.22^{+0.12}_{-0.11}$	$1.21^{+0.12}_{-0.11}$	$1.26^{+0.13}_{-0.12}$
Γ	$1.49^{+0.16}_{-0.091}$	$1.63^{+0.20}_{-0.231}$	$1.90^{+0.14}_{-0.08}$
norm 10^{-4}	$3.77^{+2.26}_{-0.99}$	$5.48^{+4.15}_{-2.48}$	$9.68^{+4.20}_{-3.01}$
θ_{obs}	90°	...	87°
$\text{Log}(N_{\text{H,LOS}})$	$23.54^{+0.06}_{-0.06}$	$23.55^{+0.07}_{-0.06}$	$23.58^{+0.04}_{-0.04}$
$\text{Log}(N_{\text{H,tor}})$	$=\text{Log}(N_{\text{H,LOS}})$	$23.97^{+0.45}_{-0.83}$	24.2°
A_S	$1.35^{+1.06}_{-0.81}$	1.00°	...
f_c	0.50°	...	$1.00^{+0.00u}_{-0.37}$
$f_s 10^{-2}$	$0.2^{+0.3}_{-0.1}$	$0.2^{+0.2}_{-0.1}$	<0.2
F_{2-10}	$6.14^{+0.21}_{-1.37}$	$6.13^{+0.32}_{-3.51}$	$5.88^{+0.32}_{-1.36}$
F_{15-55}	$46.71^{+3.15}_{-13.75}$	$44.56^{+3.12}_{-18.72}$	$42.94^{+9.79}_{-15.01}$
$\text{Log}(L_{2-10})$	$43.25^{+0.25}_{-0.75}$	$43.33^{+0.25}_{-0.64}$	$43.40^{+0.25}_{-0.64}$
$\text{Log}(L_{15-55})$	$43.64^{+0.24}_{-0.66}$	$43.48^{+0.24}_{-0.79}$	$43.24^{+0.23}_{-0.44}$

Note. $C_{\text{Ins}} = C_{\text{NuS}/\text{XMM}}$ is the cross calibration between *NuSTAR* and *XMM-Newton*, z is the source redshift, Γ is the power-law photon index, norm is the main power-law normalization at 1 keV, in units of photons $\text{s}^{-1} \text{cm}^{-2} \text{keV}^{-1}$, $N_{\text{H,eq}}$ is the equatorial column density, in units of cm^{-2} , θ_{obs} is the inclination angle between the observer LOS and the torus axis, A_S is the intensity of the reprocessed component, f_s is the fraction of emission scattered, rather than absorbed by the obscuring torus, and kT is the temperature (in keV) of the phenomenological *mekal* component used to fit the excess at <1 keV. $N_{\text{H,LOS}}$ is the LOS column density, while $N_{\text{H,S}}$ and $N_{\text{H,tor}}$ are the average torus column densities as measured using *MYTorus* decoupled and *borus02*, respectively, and f_c is the torus covering factor, $f_c = \cos(\theta_{\text{tor}})$. Finally, F_{2-10} and F_{15-55} are the observed fluxes (in units of $10^{-13} \text{erg cm}^{-2} \text{s}^{-1}$) in the 2–10 and 15–55 keV bands, while L_{2-10} and L_{15-55} are the intrinsic luminosities (in units of erg s^{-1}) in the same bands.

using *borus02* ($\Gamma = 1.90^{+0.14}_{-0.08}$), while the LOS column density is in full agreement with those measured using *MYTorus*, being $\text{Log}(N_{\text{H,LOS}}) = 23.58^{+0.04}_{-0.04}$, and the average torus column density corresponding to the minimum χ^2 ($\text{Log}(N_{\text{H,tor}}) = 24.2$) is consistent with the one measured

with “*MYTorus* coupled.” Based on the *borus02* results, 2MASX J10313591–4206093 has a large covering factor, $f_c = 1.00^{+0.00}_{-0.37}$. A large covering factor implies a larger contribution of the reprocessed emission to the overall spectrum at energies above 10 keV (as shown in Figure 4, right panel), and explains the softer photon index we find using *borus02*. Given the better χ^2 , we assume that the *borus02* best fit offers the most reliable characterization of 2MASX J10313591–4206093.

In summary, the joint *NuSTAR*–*XMM-Newton* spectral analysis allows us to reliably claim that 2MASX J10313591–4206093 is a fairly luminous ($L_{2-10} = 1.5\text{--}2.5 \times 10^{43} \text{erg s}^{-1}$), heavily obscured, albeit non-CT AGN.

ORCID iDs

S. Marchesi  <https://orcid.org/0000-0001-5544-0749>
M. Ajello  <https://orcid.org/0000-0002-6584-1703>
X. Zhao  <https://orcid.org/0000-0002-7791-3671>
A. Comastri  <https://orcid.org/0000-0003-3451-9970>
V. La Parola  <https://orcid.org/0000-0002-8087-6488>

References

- Ajello, M., Greiner, J., Sato, G., et al. 2008, *ApJ*, 689, 666
Ananna, T. T., Treister, E., Urry, C. M., et al. 2019, *ApJ*, 871, 240
Anders, E., & Grevesse, N. 1989, *GeCoA*, 53, 197
Annuar, A., Gandhi, P., Alexander, D. M., et al. 2015, *ApJ*, 815, 36
Antonucci, R. 1993, *ARA&A*, 31, 473
Araud, K. A. 1996, in ASP Conf. Ser. 101, *Astronomical Data Analysis Software and Systems V*, ed. G. H. Jacoby & J. Barnes (San Francisco, CA: ASP), 17
Ballantyne, D. R., Draper, A. R., Madsen, K. K., Rigby, J. R., & Treister, E. 2011, *ApJ*, 736, 56
Baloković, M., Brightman, M., Harrison, F. A., et al. 2018, *ApJ*, 854, 42
Baloković, M., Comastri, A., Harrison, F. A., et al. 2014, *ApJ*, 794, 111
Bauer, F. E., Arévalo, P., Walton, D. J., et al. 2015, *ApJ*, 812, 116
Brightman, M., Baloković, M., Ballantyne, D. R., et al. 2017, *ApJ*, 844, 10
Brightman, M., Baloković, M., Stern, D., et al. 2015, *ApJ*, 805, 41
Brightman, M., & Nandra, K. 2011, *MNRAS*, 413, 1206
Burlon, D., Ajello, M., Greiner, J., et al. 2011, *ApJ*, 728, 58
Comastri, A., Setti, G., Zamorani, G., & Hasinger, G. 1995, *A&A*, 296, 1
Elvis, M., Wilkes, B. J., McDowell, J. C., et al. 1994, *ApJS*, 95, 1
Furui, S., Fukazawa, Y., Odaka, H., et al. 2016, *ApJ*, 818, 164
Gilli, R., Comastri, A., & Hasinger, G. 2007, *A&A*, 463, 79

- Harrison, F. A., Craig, W. W., Christensen, F. E., et al. 2013, *ApJ*, **770**, 103
- Ikeda, S., Awaki, H., & Terashima, Y. 2009, *ApJ*, **692**, 608
- Jansen, F., Lumb, D., Altieri, B., et al. 2001, *A&A*, **365**, L1
- Kalberla, P. M. W., Burton, W. B., Hartmann, D., et al. 2005, *A&A*, **440**, 775
- Koss, M. J., Assef, R., Baloković, M., et al. 2016, *ApJ*, **825**, 85
- Koss, M. J., Romero-Cañizales, C., Baronchelli, L., et al. 2015, *ApJ*, **807**, 149
- Liu, Y., & Li, X. 2014, *ApJ*, **787**, 52
- Lusso, E., Comastri, A., Simmons, B. D., et al. 2012, *MNRAS*, **425**, 623
- Marchesi, S., Ajello, M., Marcotulli, L., et al. 2018, *ApJ*, **854**, 49
- Marchesi, S., Ajello, M., Zhao, X., et al. 2019, *ApJ*, **872**, 8
- Marchesi, S., Lanzuisi, G., Civano, F., et al. 2016, *ApJ*, **830**, 100
- Marconi, A., Risaliti, G., Gilli, R., et al. 2004, *MNRAS*, **351**, 169
- Masini, A., Comastri, A., Baloković, M., et al. 2016, *A&A*, **589**, A59
- Mewe, R., Gronenschild, E. H. B. M., & van den Oord, G. H. J. 1985, *A&AS*, **62**, 197
- Murphy, K. D., & Yaqoob, T. 2009, *MNRAS*, **397**, 1549
- Nandra, K., & Pounds, K. A. 1994, *MNRAS*, **268**, 405
- Puccetti, S., Comastri, A., Bauer, F. E., et al. 2016, *A&A*, **585**, A157
- Puccetti, S., Comastri, A., Fiore, F., et al. 2014, *ApJ*, **793**, 26
- Ricci, C., Ueda, Y., Koss, M. J., et al. 2015, *ApJL*, **815**, L13
- Risaliti, G., & Elvis, M. 2004, in *Supermassive Black Holes in the Distant Universe*, ed. A. J. Barger (Dordrecht: Kluwer Academic Publishers), 187
- Rivers, E., Baloković, M., Arévalo, P., et al. 2015, *ApJ*, **815**, 55
- Segreto, A., Cusumano, G., Ferrigno, C., et al. 2010, *A&A*, **510**, A47
- Treister, E., Urry, C. M., & Virani, S. 2009, *ApJ*, **696**, 110
- Ueda, Y., Akiyama, M., Hasinger, G., Miyaji, T., & Watson, M. G. 2014, *ApJ*, **786**, 104
- Ursini, F., Bassani, L., Panessa, F., et al. 2018, *MNRAS*, **474**, 5684
- Verner, D. A., Ferland, G. J., Korista, K. T., & Yakovlev, D. G. 1996, *ApJ*, **465**, 487
- Woo, J.-H., & Urry, C. M. 2002, *ApJL*, **581**, L5
- Yaqoob, T. 2012, *MNRAS*, **423**, 3360
- Yaqoob, T., Murphy, K. D., Miller, L., & Turner, T. J. 2010, *MNRAS*, **401**, 411
- Yaqoob, T., Tatum, M. M., Scholtes, A., Gottlieb, A., & Turner, T. J. 2015, *MNRAS*, **454**, 973
- Zhao, X., Marchesi, S., & Ajello, M. 2019a, *ApJ*, **871**, 182
- Zhao, X., Marchesi, S., Ajello, M., et al. 2019b, *ApJ*, **870**, 60